

Scene dependence of the non-gaussian scaling properties of natural images

ÁNGEL NEVADO*, ANTONIO TURIEL[†] and NÉSTOR PARGA[‡]
*Departamento de Física Teórica
Universidad Autónoma de Madrid
Canto Blanco, 28049 Madrid, Spain*

Abstract

We report results on the scaling properties of changes in contrast of natural images in different visual environments. This study confirms the existence, in a vast class of images, of a multiplicative process relating the variations in contrast seen at two different scales, as was found in [4, 5]. But it also shows that the scaling exponents are not universal: Even if most images follow the same type of statistics, they do it with different values of the distribution parameters. Motivated by these results, we also present the analysis of a generative model of images that reproduces those properties and that has the correct power spectrum. Possible implications for visual processing are also discussed.

NETWORK **11** 131-152 (2000)

*E-mail: anevado@delta.ft.uam.es

†E-mail: amturiel@delta.ft.uam.es

‡To whom correspondence should be addressed. E-mail: parga@delta.ft.uam.es

1 Introduction

As it has been suggested a long time ago [1], the early stages of the visual system must have evolved by adaptation to the statistics of the external stimuli. During this process the neurons in the visual pathway have developed their receptive fields in such a way that information about visual scenes is represented internally in an efficient way. The large amount of redundancy present in the external world is, at least in part, eliminated from the internal sensory code.

In order to achieve this quasi-optimal representation the visual system must have learnt the regularities present in the environment where the organism lived. If a given conjunction of some elementary features tend to appear together, a cell responding optimally to the combination of features is rather likely to exist.

Carrying out this program requires, as a first step, to perform an analysis of the statistical properties of the environment. In the case of visual scenes, a systematic study of this matter has began rather recently [2, 3, 4, 5, 6, 7]. Although the relevance of the second order statistics has been pointed out some time ago [8, 9], and a gaussian distribution for images has very often been used [10, 11, 12, 13] to make predictions on the receptive fields of cells in V1 and in previous stages of the visual pathway, there are many reasons to believe that this statistics leaves aside a vast number of qualitatively important properties. An indication of this is that once the image is decorrelated (i.e. the correlations between pairs of pixels are eliminated) the scene can still be recognized [14], something that is mainly due to the fact that the borders of the objects are still present.

As it was emphasized in [3, 5, 6], a better understanding of the statistics of images should be achieved before making predictions on the visual system. In fact, an analysis of the properties of changes in contrast in natural scenes revealed the existence of multiscaling properties: images do not have uniform scale properties, but they can be decomposed in sets of pixels such that only those pixels in a given set have similar scale properties.¹ Interestingly enough, these properties can be explained [4, 5] by means of a simple model, that obtains the statistics of changes in contrast at a scale r in terms of an independent multiplicative process applied to the changes occurring at a larger scale L .

The multiplicative process is a log-Poisson distribution. The events it generates represent sharp changes, or modulations, of the contrast gradient. It contains two parameters: the average number of events per unit of scale, \bar{s} , and the strength of each of these elementary changes, β . For the ensembles considered in [5, 6] these parameters took the values $\bar{s} \approx 1$. and $\beta \approx 0.5$.²

The set of images used for those studies was rather uniform, they were generally forest scenes, and their contrast distribution was also similar from image to image. This fact made the statistical analysis very stable, and the existence of the multiplicative relation between different scales was clear. It left however open the question of how much dependent those properties are on the chosen image ensemble. Their

¹Image structure in scale-space has been considered by several authors, although from a perspective different from ours [15, 16].

²Similar processes also occur in the physics of turbulent flows [17, 18, 19, 20].

possible relevance for the development of the early visual system would be greatly diminished if they only held in a restricted set of images. On the other hand, if the same statistical properties of changes in contrast could be found in a large set of visual scenes, their importance would be more clear.

In this paper we address the issue of robustness of the properties of edges and softer textures analyzed in [4, 5]. In order to establish their validity we use a larger data set (more than a hundred times larger than the one used in our first analysis) and more heterogeneous images, containing many different environments.

Our result is both surprising and encouraging. The statistical analysis can be performed on an image by image basis. When this is done, one finds that most of them (375 out of 400) exhibit the scale properties found in the smaller data set. Besides, the same log-Poisson model can be applied to explain the data. That is, for most images, contrast changes at different scales are related by the same type of multiplicative process. Nevertheless, the model parameter β depends on the image.

We have also carried out a similar statistical analysis for ensembles of images, where each ensemble was characterized by the type of scenes. Again, each of the ensembles analyzed presents the same multiscaling properties, although with different values of the parameter β . Finally, we have done the study over the whole set of images, and have again found that the same model is able to explain the observed quantities.

Given these results, our conjecture is that the visual system has adapted, during a long period of time, to the existence of these multiscale properties and, in particular, that its architecture has captured the existence of the multiplicative process. On the other hand, since different visual scenes differ in the value of the parameter β , the adaptation to this should occur more rapidly, and could be implemented, for instance, by gain control mechanisms.

Stochastic generative models of images can be useful to understand the role played by the statistical properties of images in the structure of receptive fields. These models become very simple if it is assumed that only the second order statistics is relevant; in this case the contrast distribution is just a gaussian with the correct correlation function between pairs of pixels. But the definition of a model able to describe correctly the statistics of changes in contrast requires a different approach. Here we have studied a model that reproduces the properties exhibited by the natural images analyzed in the first part of this work. As we will see, it also possesses the correct power spectrum. This generative model will also allow us to see more clearly the role of the log-Poisson parameters on the geometrical structure of the images.

The layout of this paper is as follows. The next section contains a brief theoretical background about the multiplicative log-Poisson process and multifractality of images. The image data sets used in this work are described in Sec. 3, as well as the criteria that have been used to select them. The results about the statistics of changes in contrast and the existence of the multiplicative process in the various data sets are presented in Sec. 4. Sec. 5 is devoted to the presentation and analysis of a generative model of images that follows the non-gaussian statistical properties discussed in the previous sections. The last section is devoted to discussions, where the relevance of this work for the visual system is briefly discussed.

2 Multiscaling properties of images and the multiplicative process

In this section we give the basic theoretical background necessary for our numerical analysis. For further details the reader should consult the original work [4, 5, 6, 7]

2.1 The local linear edge variance

The contrast $C(\vec{x})$ is defined as $C(\vec{x}) = I(\vec{x}) - \langle I \rangle$, where $I(\vec{x})$ is the field of luminosities and $\langle I \rangle$ its average value across the image ensemble. Since we are interested in quantifying changes of the contrast $C(\mathbf{x})$ at the point \mathbf{x} and at a given scale r , it is natural to consider the following quantities [4, 5]:

$$\epsilon_{h,r}(\mathbf{x}) = \frac{1}{r} \int_{x_1}^{x_1+r} \left(\frac{\partial C(\mathbf{x}')}{\partial x'_1} \right)^2 \Bigg|_{\mathbf{x}'=\{x'_1, x_2\}} dx'_1 \quad (1)$$

and

$$\epsilon_{v,r}(\mathbf{x}) = \frac{1}{r} \int_{x_2}^{x_2+r} \left(\frac{\partial C(\mathbf{x}')}{\partial x'_2} \right)^2 \Bigg|_{\mathbf{x}'=\{x_1, x'_2\}} dx'_2 \quad (2)$$

The variables $\epsilon_{h,r}(\mathbf{x})$ and $\epsilon_{v,r}(\mathbf{x})$ are defined at the position \mathbf{x} and at a scale r . While the first takes contributions from edges transverse to a horizontal segment of size r , the second accumulates changes in contrast transverse to a vertical segment of the same size.

These variables have been interpreted as the *local linear edge variance* along the corresponding direction and at the scale r . They describe how far the changes in contrast are from being uniformly distributed in a segment, either horizontal or vertical, of size r . If these changes were constant, the estimators would be independent of r and, on the contrary, a dependence on r indicates the existence of geometrical structure. Although in this work we will discriminate between the vertical and horizontal directions, we mention that the behaviour of contrast changes at a scale r can also be studied by means of a bi-dimensional integral [6]:

$$\epsilon_r(\mathbf{x}) = \frac{1}{r^2} \int_{x_1-\frac{r}{2}}^{x_1+\frac{r}{2}} dx'_1 \int_{x_2-\frac{r}{2}}^{x_2+\frac{r}{2}} dx'_2 |\nabla C(\mathbf{x}')| \quad (3)$$

Similarly to the other two variables, $\epsilon_r(\vec{x})$ quantifies the deviation from uniform of the distribution of $|\nabla C|$.

2.2 The multiplicative process

The question now arises of how the statistics of $\epsilon_{j,l}(\mathbf{x}_0)$ (where $j = h, v$) at the scale l is related to the distribution of the variables at a larger scale L . This was discussed in [4, 5, 6] for the marginal distribution of $\epsilon_{j,r}$. The answer is simple: they are related

by a multiplicative process. Denoting by α_{lL} its associated stochastic variable, this means that

$$\epsilon_{j,l} \doteq \alpha_{lL} \epsilon_{j,L} \quad (4)$$

The random variable α_{lL} is independent of ϵ_L . The symbol \doteq indicates that the equality holds in the distributional sense, that is, both sides of the equality have the same distribution. This relation implies a linear relation between the logarithms of the variables at two different scales. This property has also been discussed in [21], although the existence of a multiplicative process was not noticed.

The process for arbitrary changes in scale was derived in [5] where it was shown that the random variable α_{lL} follows a log-Poisson process [18]. This process can be justified as follows. As the scale is gradually reduced from L to l some changes in contrast are left outside the segment of size L . But some of these changes are special in that they give rise to a singular behaviour of the derivatives of the contrast, and in turn to a discontinuity in the ϵ 's, which acquire a factor β each time that this occurs ($0 \leq \beta < 1$). We will refer to this effect by saying that a modulation has occurred. It will be assumed that:

- modulations are independent events. The average number of them contained in the change of scale ($\ln L - \ln l$) is denoted by s ,
- the image ensemble is translational invariant,
- the multiplicative process is scale invariant.

Under a finite change from L to l , there will be n modulations with probability p_n that, given the first assumption, is Poisson:

$$p_n = \frac{s^n}{n!} e^{-s} \quad (5)$$

The value of α_{lL} after n modulations is proportional to β^n : $\alpha_{lL} = \beta^n M(l, L)$. The fact that the proportionality constant is not one can be understood by noticing that if no modulations occur (i.e., $n = 0$), $\epsilon_{j,l}$ keeps as much singular structure in the interval l as that present in $\epsilon_{j,L}$, which is distributed in the larger interval L .

The dependence of $M(l, L)$ with the scales l and L can be obtained by invoking a scale invariant multiplicative process. In this case, it can only depend on the ratio l/L , that is $M(l, L) = M(\frac{l}{L})$. A standard argument shows that it has to be a power law: if the change from L to l is done through an intermediate scale r , then because of the multiplicative character of the process we have $M(\frac{l}{L}) = M(\frac{l}{r})M(\frac{r}{L})$, which can only be satisfied if $M(\frac{l}{L}) = \left(\frac{l}{L}\right)^{-\Delta}$. The exponent Δ is another parameter of the model.

Taking all these arguments into account, the distribution of $\ln \alpha_{lL}$ can be expressed as:

$$\rho_{\alpha_{lL}}(\ln \alpha_{lL}) = e^{-s} \sum_{n=0}^{\infty} \frac{s^n}{n!} \delta \left(\ln \alpha_{lL} - n \ln \beta - \Delta \ln \left(\frac{L}{l} \right) \right) . \quad (6)$$

Up to now we have considered s , β and Δ as independent parameters. However translational invariance fixes one of them. In fact, from the definition of the $\epsilon_{j,r}$'s one easily checks that its average over a translational invariant ensemble of images does not depend on r . In turn, taking the average on both sides of eq. (4), this implies that

$$\langle \alpha_{rL} \rangle = 1 \quad , \quad (7)$$

where $\langle \dots \rangle$ indicates the average over an ensemble of images. But then, imposing this condition over the value of this average obtained from the distribution in eq. (6) one has:

$$s = \frac{\Delta}{1 - \beta} \ln \frac{L}{r} \quad , \quad (8)$$

from where the average number of modulations per unit of change in scale is $\bar{s} = \frac{\Delta}{1 - \beta}$.

The existence of a multiplicative process has direct consequences on the scaling properties of the moments of $\epsilon_{j,r}$. Let us denote these moments by $\langle \epsilon_{j,r}^p \rangle$. If the log-Poisson model holds, then from eq. (6) it is easy to check that the moments have a property called Self-Similarity (SS),

$$\langle \epsilon_{j,r}^p \rangle = A_p r^{\tau_p} \quad , \quad (9)$$

where the τ_p 's are the SS exponents. Notice that this also implies that any moment can be expressed as a power of the moment of order q . Choosing $q = 2$ this means that

$$\langle \epsilon_{j,r}^p \rangle = A(p, 2) \left[\langle \epsilon_r^2 \rangle \right]^{\rho(p, 2)} \quad , \quad (10)$$

This relation could hold even when SS is not true. It is called Extended Self-Similarity (ESS) [25]. The $\rho(p, 2)$'s are the ESS exponents and the $A(p, 2)$'s are geometrical factors. The exponents $\rho(p, 2)$ can be predicted using the distribution of the multiplicative process, eq. (6), to evaluate the moments of order p in eq. (4). This computation yields

$$\rho(p, 2) = \frac{p}{1 - \beta} - \frac{1 - \beta^p}{(1 - \beta)^2} \quad . \quad (11)$$

Let us notice that although the model has two parameters, β and \bar{s} , the ESS exponents $\rho(p, 2)$ depend only on the modulation parameter β . There is a simple relation between τ_p and $\rho(p, 2)$:

$$\tau_p = -\bar{s}(1 - \beta)^2 \rho(p, 2) \quad , \quad (12)$$

Conversely, it can be proven that if SS and ESS hold and the exponents $\rho(p, 2)$ verify eq. (11), then ϵ_r can be described in terms of a multiplicative process (eq. (4)) of the log-Poisson type (eq. (6)). It is then enough to check eq. (11), from where the existence of a log-Poisson process is derived.

2.3 Multifractality of images

The process just described has an interesting geometrical interpretation, as has been discussed in [6]. In fact, the power law behaviour of the moments $\langle \epsilon_{j,r}^p \rangle$, given in eq. (9), can be traced back to the existence of a very irregular behaviour of $\epsilon_r(\vec{x})$, which can be expressed as:

$$\epsilon_r(\vec{x}) = \alpha(\vec{x}) r^{h(\vec{x})} , \quad (13)$$

where the exponent $h(\vec{x})$ depends on the site of the image. This property is, in turn, related to a singular behaviour of $|\nabla C|(\vec{x})$: $h < 0$ indicates a divergence of $|\nabla C|(\vec{x})$ to infinity, while $h > 0$ indicates finiteness and continuous behavior. The greater the exponent the smoother is the the change in contrast around that point. Eq. (13) expresses that all the points are singular (in this wide sense), and that the singularity exponent is not uniform. This property allows to classify the pixels in a given image: the set of points with a singularity exponent contained in the interval $[h - \Delta_h, h + \Delta_h]$ (where Δ_h is a small positive number) define a class F_h . These classes are the *fractal components* of the image (the notion of fractality is discussed in [23, 24]). The smaller the exponent the more singular is the class, and the most singular component is the one with the smallest value of h . A mathematical object with this structure is said to be a *multifractal*, a concept originally introduced in the context of fully developed turbulence [22].

The irregular arrangement of pixels in a fractal component F_h can be characterized by counting the number of pixels contained inside a given ball of radius r , $N_r(h, \Delta_h)$. As $r \rightarrow 0$ it is verified that

$$N_r(h, \Delta_h) \sim r^{D(h)} . \quad (14)$$

This exponent $D(h)$ quantifies the size of the set of pixels with singularity h as the image is covered with small balls of radius r . It is the fractal dimension of the associated fractal component F_h , and the function $D(h)$ is called the *singularity spectrum* of the multifractal [22].

There is an important connection between the local singularity analysis and the statistical description of the image in terms of the moments $\langle \epsilon_{j,r}^p \rangle$. In fact, the ESS exponents τ_p are the Legendre transform of the singularity spectrum $D(h)$ ([22], see also [6]),

$$D(h) = \min_p \{ph + d - \tau_p\} , \quad (15)$$

where $d = 2$ is the dimensionality of the images. Given the τ_p 's, eqs. (12) and (11), the dimension spectrum can be predicted:

$$D(h) = D_\infty - \frac{h + \Delta}{\ln \beta} \left[1 - \ln \left(-\frac{h + \Delta}{(d - D_\infty) \ln \beta} \right) \right] , \quad (16)$$

where D_∞ is defined as $D_\infty = d - \bar{s}$. From here one notices that there is a minimum value of the singularity exponent h , given by $h = -\Delta$ which then is the singularity of the most singular fractal component. Its fractal dimension can be computed from

eq. (16) which yields $D(-\Delta) = D_\infty$. Then D_∞ is the dimension of the most singular set; it can be expressed in terms of the parameters of the model, e.g. β and Δ , as

$$d - D_\infty = \bar{s} = \frac{\Delta}{1 - \beta} . \quad (17)$$

The points with the strongest singularity ($h = -\Delta$) are those with the sharpest changes in contrast (edges). This can be explicitly verified by evaluating the singularity exponents of all the pixels in the image and extracting those with the minimum value of h (within a resolution Δ_h) [6]. Let us remark that the most singular points could have a rather weak singularity, but even in these cases they are the points where the most important changes in contrast occur. This happens, in particular, when there are no modulations ($\bar{s} = 0$ or, equivalently, $D_\infty = 2$), in which case $\Delta = 0$.

The parameter β was defined as the strength of a modulation in the multiplicative process, but it can also be interpreted in terms of the geometrical properties of the edges in the image. In fact, eq. (17) relates β with D_∞ and Δ , which describe properties of the set of pixels where the changes in contrast are most singular: $\beta = \frac{-\Delta}{2 - D_\infty} + 1$. For fixed D_∞ , as β decreases, the singularity exponent of the edges, $-\Delta$, decreases. In order to gain some intuition about this relation, let us consider an isolated jump in contrast. Its dimensionality is $D_\infty = 1$, and it can be proved³ that $\Delta = 1$, what gives $\beta = 0$. By contrast, images with statistics dominated by smooth changes of contrast have $\beta = 1$. This is so because $\Delta = 0$, but this result can also be understood by noticing that the way to obtain smooth images with the log-Poisson process is to set $\beta = 1$.

The measurable quantities are the moments $\langle \epsilon_{j,r}^p \rangle$, and from them one can obtain the SS exponents τ_p and the ESS exponents $\rho(p, 2)$. Given the experimental ESS exponents $\rho(p, 2)$, it is easy to obtain the value of β by performing a least squares regression on eq. (11). To define the log-Poisson process completely one should still estimate $D_\infty = 2 - \bar{s}$, which can be done for instance using the measured value of τ_2 . This can be seen from eq. (12) which after setting $p = 2$ yields

$$D_\infty = 2 - \frac{\tau_2}{(1 - \beta)^2} . \quad (18)$$

Let us remark that this expression contains a dependence in $1/(1 - \beta)^2$ which makes the propagation of errors important as β approaches the value one, even if the uncertainty in the values of β and τ_2 are small.

3 Choice of environments

In the present study we used a data set of 200 images, having 1536×1024 pixels and 16 bits in luminance depth. These images have been kindly provided to us by Hans van Hateren [28] and were selected from his data set of about 4200 images. The selected images can be observed and downloaded from the URL address <http://hlab.phys.rug.nl/archive.html>. A list of them is provided in Table 1. The files

³see, e.g., [6]

are originally named as “IMK#.IMC”. In the table only the number (#) of the corresponding image is specified.

To compare with previous studies we notice that the images used in [5] contained 45 natural scenes with a size of 256×256 pixels and a luminance depth of 13 bits. This means that our present statistical database has 130 times as many bits as the previous one.

The data set has been considered either complete or divided into four different subsets with 50 images in each of them. These four ensembles were selected to meet the following requirements:

- Ensemble A:

It contains natural scenes of trees and woods. The images do not have artificial objects or open skies. The woods are dense and neither shadows nor direct light rays are allowed.

- Ensemble B:

It contains natural scenes. The rest of conditions imposed in the definition of ensemble A have not been required here.

- Ensemble C:

Images containing both artificial and natural objects are included. We chose images that in a visual scan appear to have predominantly horizontal structures, i.e, the horizontal edges seem to be longer than the vertical ones. We are interested in testing whether this implies a difference between the horizontal and vertical statistics.

- Ensemble D:

Out of the whole database of 4212 images in [28] we picked up 50 randomly. No image belonging to any of the other three ensembles was included here. The intention is to have a data set as varied as possible.

Each ensemble is used to study the vertical and the horizontal statistics (that is the marginal statistics of $\epsilon_{h,r}(\mathbf{x})$ and $\epsilon_{v,r}(\mathbf{x})$, respectively), what gives a total of eight different elements.

4 Results

The main purpose of this section is to establish whether the statistical properties of SS and ESS, eqs.(9, 10), are present in the ensembles considered, and whether the ESS exponents can be predicted by the log-Poisson model, eq.(6). This will be done taking three different categories of ensembles. In Sec. 4.2 we consider the four ensembles defined in Sec. 3 for the horizontal and vertical directions. Next, in Sec. 4.3 we take as ensembles the individual images themselves, again for both directions. Finally in Sec. 4.4 we regard the 200 images as a single ensemble and we accumulate

Ensemble	Image number
A	0034, 0211, 0263, 0478, 0586, 0605, 0662, 0683, 0801, 0808
	0881, 1017, 1031, 1164, 1406, 2035, 2263, 2280, 2411, 2417
	2603, 2605, 2606, 2626, 2649, 2935, 3002, 3134, 3491, 3514
	3536, 3789, 3807, 3830, 3842, 3940, 4010, 4031, 4037, 4042
	4044, 4056, 4069, 4078, 4094, 4098, 4101, 4123, 4133, 4134
B	0037, 0071, 0222, 0265, 0511, 0758, 0774, 0807, 0836, 0877
	1206, 1341, 1375, 1814, 1831, 1836, 1852, 1867, 1889, 1926
	1976, 1992, 2071, 2159, 2214, 2409, 2437, 2619, 2623, 2805
	2806, 3236, 3269, 3318, 3414, 3415, 3611, 3615, 3635, 3913
	4028, 4066, 4087, 4089, 4107, 4121, 4122, 4139, 4184, 4193
C	0001, 0038, 0046, 0052, 0085, 0090, 0127, 0145, 0146, 0147
	0168, 0177, 0210, 0403, 0423, 0459, 1282, 1357, 1400, 1411
	1423, 1427, 1431, 1432, 1471, 1489, 1529, 1562, 1566, 1600
	1878, 1879, 1934, 1946, 1950, 1964, 3029, 3054, 3065, 3082
	3099, 3137, 3154, 3179, 3223, 3225, 3286, 3322, 3332, 3384
D	0288, 0325, 0342, 0446, 0609, 0668, 0685, 0695, 0850, 0879
	0914, 0920, 1092, 1171, 1191, 1201, 1249, 1322, 1414, 1422
	1462, 1645, 1691, 1775, 1945, 2231, 2235, 2499, 2582, 2749
	2750, 2770, 3079, 3123, 3181, 3214, 3356, 3474, 3496, 3540
	3546, 3680, 3752, 3784, 3786, 3894, 3952, 3988, 4058, 4086

Table 1: The 200 selected images and its classification in the four ensembles A-D

the horizontal and vertical statistics in the same distribution. Notice that the moments are self-averaging quantities but the ESS exponents, and therefore the parameter β of the probability distribution of eq. (6) are not, so we do not expect the parameter β of an ensemble to be the average of the β 's of its images.

4.1 Methods

Here we describe the methods used to check the presence of SS, ESS and the log-Poisson model for given p -moments of ϵ_r . The statistical moments will be computed over the three different categories we are going to analyze, i.e., for each of the eight orientational ensembles, for single images and for the whole data set. The items of a category giving rise to the different moments $\langle \epsilon_r^p \rangle$ will be referred to as elements. (Hence, we have eight elements in the first category, 400 in the second and just one in the third).

The existence of SS will be checked by verifying that $\ln \langle \epsilon_{j,r}^p \rangle$ is linear in $\ln r$ for each element (the symbol $\langle . \rangle$ denotes the ensemble average over the images belonging to that element). In order to present the results for different elements in a single graph and to evaluate the standard deviation of the data, we have proceeded as follows. Since each element has its own scaling exponents the curves have to be

normalized; we first define,

$$S_p(x) = \ln \langle \epsilon_{j,r}^p \rangle , \quad (19)$$

where $x = \ln r$. When $S_p(x)$ vs x is fitted by a least-squares regression it yields the fitting line ⁴: $\hat{S}_p(x) = a + bx$. We now perform a linear transformation $\hat{S}_p \rightarrow \hat{S}'_p$ such that $\hat{S}'_p = x$ for each ensemble. The same transformation is applied to $S_p(x)$ to give

$$S_p(x) \rightarrow S'_p(x) = \frac{S_p(x) - a}{b} . \quad (20)$$

The average over different S'_p of a given category can now be carried out, yielding the quantities \bar{S}'_p . ESS is analyzed in a similar way; now we define

$$E_p(y) = \ln \langle \epsilon_{j,r}^p \rangle \quad (21)$$

where $y = \ln \langle \epsilon_{j,r}^2 \rangle$. The fitting line for each element is expressed as $\hat{E}_p(y) = c + d y$. However now not only the fit parameters c and d depend on the element considered, but also the variable y , for fixed r , varies from element to element. Therefore, before transforming all the fitting lines onto a common function, one has to normalize y properly. This is done as:

$$y \rightarrow y' = \frac{y - y_{min}}{y_{max} - y_{min}} \quad (22)$$

where y_{max} and y_{min} are respectively the maximum and minimum values of y for a given element. This maps y into the interval [0:1]. As before we apply to E_p the transformation that yields $\hat{E}_p \rightarrow \hat{E}'_p = y'$:

$$E_p \rightarrow E'_p(y') = \frac{E_p(y) - (a + by_{min})}{b(y_{max} - y_{min})} . \quad (23)$$

The experimental ESS exponents $\rho(p, 2)$ for each element in the category are fitted by a least-squares regression. An important result is that each element follows the log-Poisson model although the optimal value of β varies from element to element. To represent the data from all the elements together we define a normalized $\rho'(p, 2)$ as:

$$\rho'(p, 2) = \frac{\rho(p, 2)}{\rho^\beta(p, 2)} \rho^{\beta_0}(p, 2) \quad (24)$$

where $\rho(p, 2)$ denotes the computed ESS exponents ⁵ obtained from each element, ρ^β denotes the exponents predicted by the log-Poisson model (11) using the value of β

⁴Notice that the fitting parameter b gives an estimate of the SS exponent τ_p . The linear regression is performed in the range $r = [8 : 25]$, where the SS property is best realized

⁵These exponents are obtained with a linear regression of the ESS curves for each moment. This regression is performed in the range $r = [8 : 25]$, where also the ESS property is best realized. The function $\rho(p, 2)$ is computed up to $p = 7$. For higher order moments the properties of SS and ESS begin to appear less clearly. The reason for this is that the main contribution to these moments comes from the tail of the distribution of $\epsilon_{r,l}$, where the sampling is worse.

that best fits the data and $\rho^{\beta_0}(p, 2)$ are the exponents predicted by the log-Poisson model with a certain β_0 conventionally set equal to 0.5. (i.e., half of its maximum value).

4.2 Ensembles

We study the properties of the four ensembles in the two directions, which gives us eight elements altogether. Figs. 1Ia and 1Ib show the mean $\bar{S}'_p(x)$ and the standard deviation $\sigma_{S'_p(x)}$ for $p = 2$ and 7. It is observed that SS holds rather well, although there appear small deviations for the lowest and highest values of x .

The values of $E'_p(y')$ are plotted together for the eight elements as a function of y' . This time we cannot average over the values of $E'_p(y')$, since y' varies from element to element. Figs. 1IIa and 1IIb for $p = 2$ and 7, respectively, show that ESS holds better than SS.

Fig. 2 represents the mean value $\bar{\rho}'(p)$ over the eight ensembles as a function of p and its standard deviation. It is observed that the log-Poisson model is very well satisfied. In Table 2, the observed values of β are given. There are important numerical differences among them. As we will see in the next section this also occurs when the images are analyzed individually.

Ensemble and orientation	β
A horizontal	0.17
A vertical	0.022
B horizontal	0.27
B vertical	0.14
C horizontal	0.10
C vertical	0.10
D horizontal	0.28
D vertical	0.030

Table 2: Values of β for the four ensembles A-D and two orientations

In most of the entries of Table 2 there is an anisotropy between the observed values of β along the horizontal and vertical directions. For instance, in ensemble A the horizontal β is much larger than the vertical one. A difference between the two β 's is still present in ensemble B, although it is smaller. Both are dominated by vertical statistics (they are made up of images of woods), which somehow is reflected in the different values observed for β along each direction. However, ensemble B is more isotropic. This can be due to the existence in this ensemble of structures not present in A such as shadows, open skies and clouds, and to the fact that the woods are not as dense as in A.

Naively, one would expect a difference of the opposite sign in ensemble C, which was defined to be dominated by horizontal statistics. However, this particular ensemble reveals to be the most isotropic of the four. This apparent contradiction is

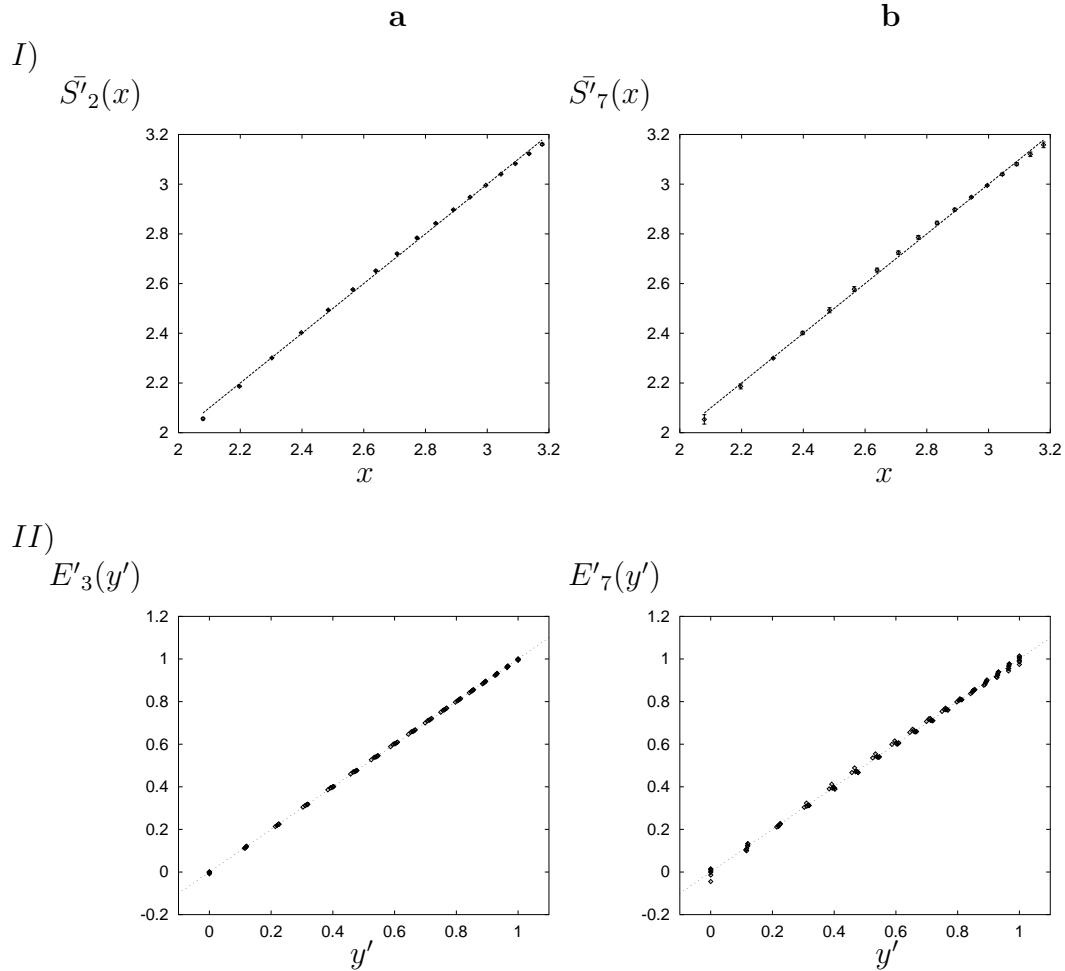


Figure 1: Test of SS and ESS for the eight ensembles. I) SS for the moments of order 2 (a) and 7 (b). The dashed line is $f(x) = x$. The diamonds represent the mean and the (small) bars the standard deviation over the eight elements. II) ESS for the moments of order 3 (a) and 7 (b). The dotted line is $f(y') = y'$

explained by the fact that even when changes in contrast along the horizontal direction are normally smooth, they present very localized fluctuations that contribute to $\epsilon_{h,r}$. In fact, a closer inspection of the images in ensemble C shows that although the contrast is more correlated along the horizontal direction, the edges appear isotropically distributed. Finally, ensemble D behaves similarly to A, except for the numerical values of β .

The values of β in Table 2 also inform of the singularity exponents of the edges, $-\Delta$ (cf. end of Sec. (2.3)). For instance, and assuming that $D_\infty \sim 1$, the small values of β in the table indicate that the corresponding statistics is dominated by sharp contrast changes. This effect is more noticeable in the vertical variable than in the horizontal one.

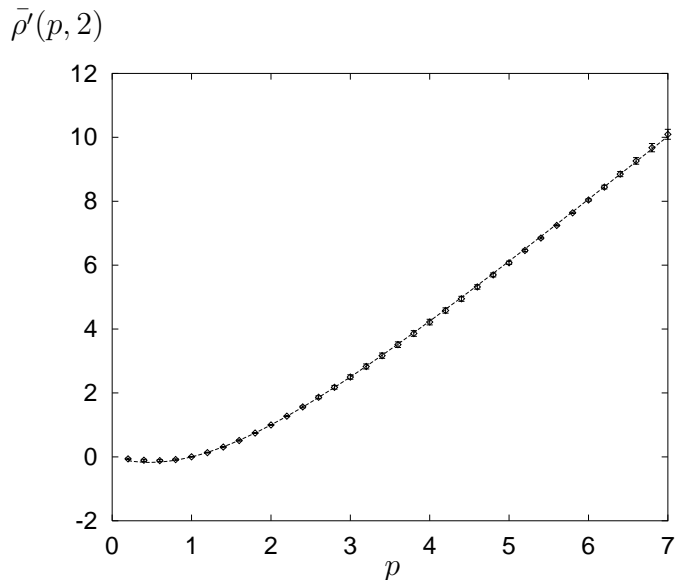


Figure 2: Test of the log-Poisson model for the eight ensembles. The diamonds represent the mean of $\rho'(p, 2)$ over the eight ensembles as a function of p and the error bars are twice the standard deviation. These error bars are small and difficult to appreciate. The dashed line represents $\rho^{0.5}(p, 2)$, the log-Poisson $\rho(p, 2)$ with $\beta = 0.5$.

4.3 Single images

Again, our aim is to establish whether the statistical properties of SS and ESS are present but this time in single images, and whether the ESS exponents can be predicted by a log-Poisson model for each of them. Now the moments $\langle \epsilon_{r,l}^p \rangle$ are obtained by averaging over the pixels of each individual image. Note that the resulting exponents $\rho(p, 2)$ of the images of a certain ensemble do not necessarily average to the ensemble exponents. This is checked for the set of 200 images for both the horizontal and vertical direction. From now on we shall refer to this set as containing 400 “images”, implying that we consider the statistics from the horizontal and the vertical directions.

The results for SS, ESS and the ESS exponents are presented applying the procedures described in Sec. 4.1. Fig. 3) shows the data for SS and ESS while Fig. 4 includes the verification that the log-Poisson model is satisfied and the corresponding distribution of values of β and D_∞ .

The means \bar{S}_p^i and $\bar{\rho}(p, 2)$ are not over the 400 images but over the 375 images that best satisfy the log-Poisson model. Of the other 25 images (6.2%), 6 of them (1.5%), have been discarded because their β exceeds 1, the maximum admissible one. The rest have been discarded because the log-Poisson model fits their $\rho(p, 2)$ significantly less accurately than that of the 375 selected images. This can be seen in Figs. 4Ia and 4Ib. The 375 images with smallest $\chi^2 = \sum_{p=1}^n (\rho(p, 2) - \rho^\beta(p, 2))^2$ are a homogeneous set in the sense that discarding a few of the worst of them produces a small improvement

of the overall fit represented in Fig. 4Ib. On the contrary, discarding the 25 worst images of the complete set produces a significant improvement of the overall fit. The discarded images have some features in common. Almost all of them either are obscure and therefore lack definition or are scenes with little structure: sea, rivers, ground with little more than grass, buildings with simple repeating patterns.

Fig. 4IIa shows that the probability of β decreases approximately linearly with β . The corresponding histograms for the eight ensembles considered in Sec. (4.2) have a similar shape, though more irregular. They extend also over the whole range [0:1]. The histograms of the vertical ensembles are peaked at a lower value of β (~ 0.05) than the horizontal ones (~ 0.25), except for ensemble C, which is in accordance with the global values of β for these ensembles, shown in Table 2.

The fractal dimension of the set of edges, D_∞ , can be estimated from eq.(18) by measuring β and τ_2 . As has already been mentioned in section (2.3), the evaluation of this fractal dimension becomes difficult for large β . In fact, D_∞ has unrealistic negative values for about 23% of the images which satisfy the log-Poisson model (all of them have $\beta > 0.5$). This can be explained by the fact that, for large β , Eq.(18) propagates errors in the estimation of β and τ_2 as very large errors in the estimation of D_∞ , due to the factor $\frac{1}{(1-\beta)^2}$. Furthermore, even if errors in β are not biased, eq.(18) gives an estimation of D_∞ biased towards lower values ⁶, which may explain why, for some images, the dimension of the most singular fractal component (the set of edges) is negative.

The result is shown in Fig. 4IIb. Notice that it is consistent with the expectation that the fractal dimension of the set of pixels with the largest changes in contrast should be close to one. Even if this histogram seems to be rather broad, a visual inspection of the fractal component corresponding to an image with, say, $D_\infty = 1.3$ looks like a not too thick line.

4.4 Whole data set

We now perform the same analysis on the global data set containing the whole set of 200 images. These are again treated as 400 “images” by averaging together the moments for the horizontal and vertical variables ϵ . The results are presented in terms of the same quantities (eqs. (20) to (24)) used in Sec. 4.1 to allow for direct comparison. The value of β obtained from this set is 0.17. Fig. 5 shows the SS test for the moments of order two and seven and the ESS test for the moments of order three and seven. The fit of the ESS exponents with a log-Poisson curve is presented in Fig. 6 (Notice that, following the convention defined in eq. (24) the curve is referred to $\beta_0 = 0.5$). It can be seen that also for the whole data set all these properties are well confirmed. Again ESS holds better than SS.

⁶This can be seen by calculating the propagated error in D_∞ to second order in the error in β . For large enough β this order becomes relevant: $\delta D_\infty = \frac{\tau_2}{(1-\beta)^3} [2\delta\beta + \frac{3}{(1-\beta)}(\delta\beta)^2]$

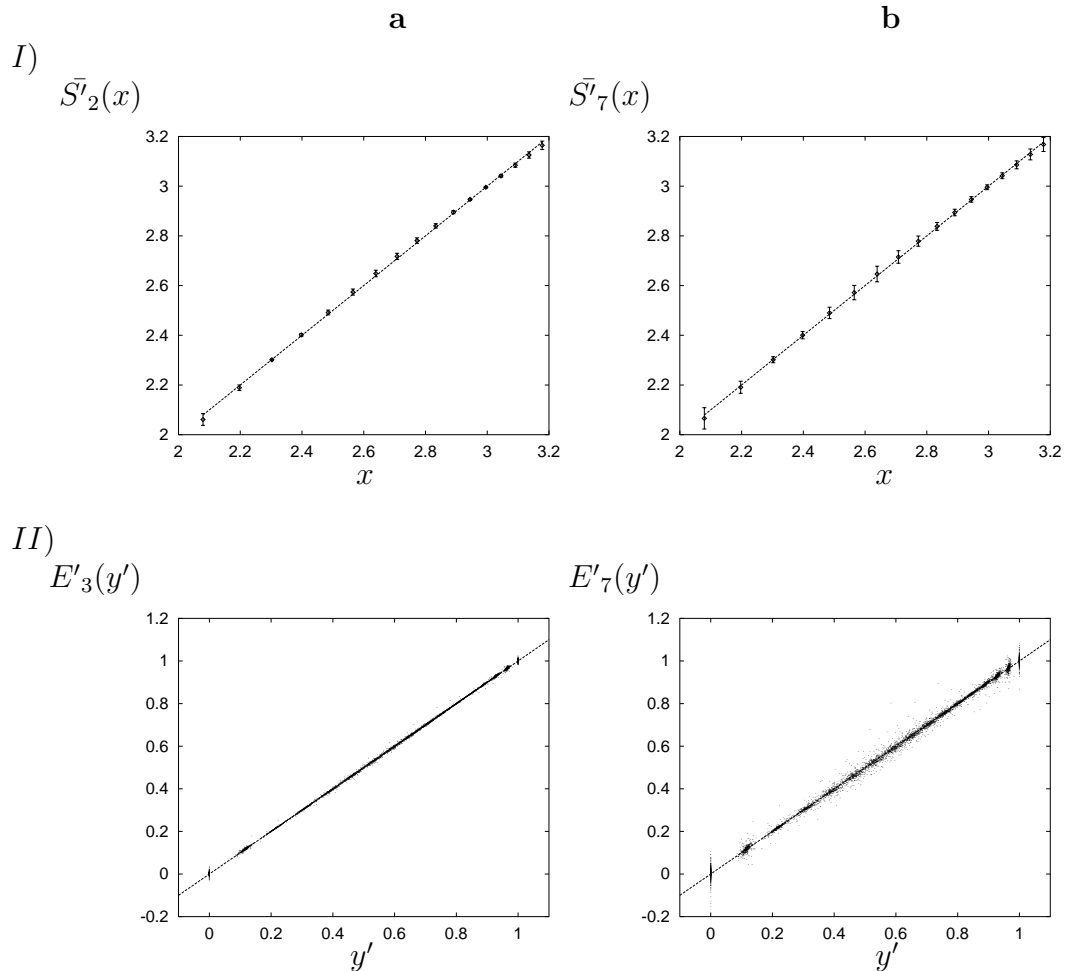


Figure 3: Test of SS and ESS for the 375 out of 400 chosen images. I) SS for the moments of order 2 (a) and 7 (b). The dashed line is $f(x) = x$. II) ESS for the moments of order 3 (a) and 7 (b). The dashed line is $f(y') = y'$

5 Generative model of images

The fact that the SS exponents τ_p do not behave linearly with p implies that scale-invariance of natural images is rather subtle. It is related to the fact that for a given image not all the points transform in the same way under scale transformations [6]. As was shown in Sec. (2.3), the log-Poisson model, which explains the non-linear behaviour of τ_p , also predicts the existence of a multifractal structure: the image pixels can be decomposed in fractal components such that points in the same component have the same scaling properties.

Generative models of natural images based on their scale properties should take this important property into account. The intuitive model proposed in [29] puts the emphasis in reproducing the correct power spectrum, but it does it in such a way that all the points have the same scale properties. This is because all the changes in contrast are sharp, and equally singular, what gives rise to a single fractal component.

An evaluation of the SS exponents τ_p would show that these are linear in p .

Here we address the issue of how to define a simple stochastic model for image generation which takes into account the properties discussed in the previous sections and that has the correct power spectrum. The model described below is based on a wavelet expansion of the contrast $C(\vec{x})$ itself. Although generative models of images based on a wavelet expansion have been proposed before (see, e.g., [30]), the existence of a multiplicative process associated with the wavelet coefficients was noticed more recently in [6]. According to this result, the multifractal structure described in section (2.3) is produced through a convenient stochastic process for the wavelet coefficients.

⁷

We will express the contrast $C(\vec{x})$ of the image in terms of a dyadic wavelet set [33] $\Psi_{j,\vec{k}}(\vec{x}) \equiv \Psi(2^j\vec{x} - \vec{k})$, where the scale r is given by $r = 2^{-j}$ ($j \in \mathcal{Z}$), and the space is sampled at the points $\vec{x}_0 = 2^{-j}\vec{k}$, with $\vec{k} \equiv (k_1, k_2)$ (k_1 and k_2 are integer numbers taking values from 0 to $2^j - 1$).

$$C(\vec{x}) = \sum_{j=0}^N \sum_{k_1, k_2=0}^{2^j-1} \gamma_{j,\vec{k}} \Psi_{j,\vec{k}}(\vec{x}) . \quad (25)$$

where N is the number of scales considered; thus, the number of pixels of the image is $2^N \times 2^N$ (each change in scale is of size 2). Synthetic images will be generated with $N = 8$, which gives rise to images with 256×256 pixels. The mother wavelet $\Psi(\vec{x})$ will be taken as the Laplacian of a gaussian with zero mean and standard deviation one. ⁸

The wavelet coefficients $\gamma_{j,\vec{k}}$ are then generated following a hierarchical procedure which starts at the scale with the poorest resolution ($j = 0$), which is described by the mother wavelet. Its coefficient, $\gamma_{0\vec{0}}$, will appear just as a normalization of the contrast level. It is then used to generate the coefficients $\gamma_{1,\vec{k}}$ ($k_1, k_2 = 0, 1$) of the wavelets located at the four points used to sample the next scale ($j = 1$). They are of the form $\gamma_{1,\vec{k}} = \alpha_{1\vec{k}}\gamma_{0\vec{0}}$, where the $\alpha_{1\vec{k}}$'s are independent, identically distributed random variables which follow a given probability distribution (to be given below). This operation is repeated recursively at every new scale. At the scale $j - 1$ each $\gamma_{j-1,\vec{k}}$ generates, by multiplication by the corresponding independent α 's, four new coefficients at the scale j :

$$\gamma_{j\vec{k}} = \frac{1}{2} \alpha_{j\vec{k}} \gamma_{j-1, [\frac{\vec{k}}{2}]} \quad (26)$$

where $[\frac{\vec{k}}{2}]$ means the vector with components equal to the integer part, rounding down, of those of \vec{k} divided by 2.

The projections of such $C(\vec{x})$ over appropriate wavelets of size r possess the property of SS. Let us consider first the dual wavelet $\tilde{\Psi}$ (that is, $\langle \tilde{\Psi}_{j\vec{k}} | \Psi_{j'\vec{k}'} \rangle = 2^{-2j} \delta_{jj'} \delta_{\vec{k}\vec{k}'}$). Defining the wavelet projection $T_{\Psi}^r C(\vec{x})$ as:

⁷Although in a different context, the model has been used before in [31] to study synthetic turbulence.

⁸The interesting question of how to choose a convenient mother wavelet for a given image ensemble is not addressed here. This problem is discussed in [32]

$$T_{\tilde{\Psi}}^r C(\vec{x}) = \frac{1}{r^2} \int d\vec{y} \tilde{\Psi}\left(\frac{\vec{x} - \vec{y}}{r}\right) C(\vec{y}) \quad (27)$$

It follows from eq. (25) that:

$$\langle |T_{\tilde{\Psi}}^r C|^p \rangle = A_p^C r^{\tau_p^C} \quad (28)$$

where

$$\tau_p^C = p - \log_2 \overline{\alpha^p}, \quad (29)$$

where $\overline{\alpha^p}$ is the moment of order p of the distribution of α . Then, there exists at least the wavelet $\tilde{\Psi}$ for which the wavelet projections of C have SS, eq. (28) (in fact, all the wavelets vanishing the same number of moments define wavelet projections of C with SS of the same exponents τ_p^C). As shown in [6], this implies that also ϵ_r verifies SS (i.e. it follows eq. (9)) and there is a simple relation between the SS exponents τ_p^C and τ_p given by:

$$\tau_p = \tau_p^C - p \quad (30)$$

and using eq. (29) we obtain $\tau_p = -\log_2 \overline{\alpha^p}$. It follows that in order to obtain SS exponents τ_p according to the log-Poisson model the random the $\alpha_{j\vec{k}}$ are computed according the log-Poisson distribution eq. (6) where the ratio $\frac{L}{r}$ is 2.

We have still to check that this model has the correct second order statistics [9]. Using a 512×512 image produced with the generative model we have verified that the power spectrum is indeed of the form $S(\vec{f}) \sim 1/f^2$, for an appropriately chosen Ψ 's. The plot and the fit are exhibited in Fig. 7.

5.1 Geometrical interpretation of the generative model

Table 3 presents a catalogue of images produced with the generative model for different values of the parameters β and \bar{s} . The images have been generated in such a way that those with identical \bar{s} (shown in the same column) contains the same number of modulations for each $\alpha_{j\vec{k}}$. That is, a given site $j\vec{k}$ has a random choice of $n_{j\vec{k}}$ modulations which is the same for all the images in the column. There is also a continuous change for fixed β as \bar{s} varies, which is obtained keeping fixed the cumulative probabilities used to generate the number of modulations at a given site.

The geometrical characteristics of the images are clear from visual inspection of the figures in Table 3. The images in the column $\bar{s} = 0$ are all the same, as the possibility of having even one modulation is neglected. These images are also obtained as the limit $\beta \rightarrow 1$ (this is because for $\beta = 1$ the modulations become irrelevant, as they do not change the value of $\gamma_{j\vec{k}}$). These two cases should correspond to a uniform contrast field (the non-uniformity in the borders is due to finite size effects). For non-trivial values of \bar{s} and β the following properties are observed:

- D_∞ is directly related to \bar{s} by eq.(17): $D_\infty = 2 - \bar{s}$. Therefore, for fixed β , as \bar{s} increases D_∞ decreases, as can be seen in Table 3 going from left to right.

- As β increases at fixed \bar{s} , Δ decreases. Visually it can be appreciated that the singularity exponents decrease in Table 3 from top to bottom.

5.2 Numerical analysis of the generative model

The artificial images are constructed to have a certain theoretical β and \bar{s} . We study here the properties of 32 generated images of 256×256 pixels with $\beta = 0.40$. The histogram in Fig. 8 shows the distribution of the 64 computed β 's for the horizontal and vertical direction of each of the 32 images. The mean of the histogram is $\beta = 0.31$ with standard deviation $\sigma_\beta = 0.13$. The fluctuations around the mean and its bias with respect to the theoretical β are mainly due to the finite size of the images and not to the size of the data set. To verify this we have randomly divided the data set in two sets of 12 and 20 images and have checked that neither their means nor their standard deviations change appreciably.

On the other hand, averaging the moments of the 64 cases (which approximates very well the moments computed over a single 2048×2048 image) yields $\beta = 0.38$ (Fig. 9a), rather close to the theoretical 0.40.

What is interesting is that even when these fluctuations in β are due to finite size effects the multiplicative process for each image is preserved. This can be seen in Fig. 9b where the mean and variance of the normalized ESS exponent $\rho'(p, 2)$ (averaged over the 64 cases) is shown.

One can wonder whether the fluctuations in β observed in the true images could be thought of as finite size effects. This does not seem to be the case. As we have seen in Sec. 4.4 even the whole set of images follows the log-Poisson model with a given β . Considering this set as a single large image, each of its pieces (i.e. the single images) should follow the log-Poisson model with β 's distributed as in Fig. 8. However, if the fluctuations of the artificial images were a good model for the fluctuations of the true ones, then the dispersion of the histogram in Fig. 8 should be larger than that of the histogram in Fig. 4III (because the synthetic images are smaller than the true ones).

6 Discussion

One of the main conclusions of this work is that the multiscaling properties of changes in contrast are robust in natural scenes: Both SS and ESS are present in almost every single image considered, which are of very different type. In addition, a vast number of the images in our data set (94%) can be described in terms of a multiplicative process of the log-Poisson type. The modulation parameter β is distributed over its admissible range, although the probability distribution decreases with increasing β .

Four different ensembles of images (described in Sec. 3) were considered in order to understand how the presence or absence of certain features affects the edge statistics. The moments of the relevant variables ϵ_r were then computed by averaging over all the images in the ensemble. It was found that SS, ESS and the same multiplicative process are also present in each of the four ensembles and for both vertical and horizontal statistics. Again, these eight cases differ only in the value of β .

The same properties (SS, ESS and log-Poisson) hold when the whole data set is taken as the ensemble. We can conclude from our experimental study of the three categories of ensembles that SS, ESS and the log-Poisson model are robust features of natural images. It is very remarkable that ensembles following log-Poisson laws with different values of the parameter β can be combined together giving again a log-Poisson model.

One point that we want to emphasize is that the existence of a multiplicative process of a given type (the log-Poisson model) is very robust. It is present in images with rather different aspect, what supports the expectation that it has actually been detected by the early visual system in the course of evolution. If so, it should be contained in the structure of the receptive fields. On the other hand, there is a high variability in the value of the model parameter β . Then, when the image ensemble changes, the cell should adapt to the new value of β . This is not an unusual situation in the visual system: it adapts, for instance, to the average contrast [36, 37].

The generative model studied in this paper provides a simple way to produce images with the multiscaling properties of natural scenes. It could be used as a better description of the contrast distribution that contains not only the correct second order statistics but also a correct description of the non-gaussian aspects of changes in contrast. The model could then be used to study the consequences that these properties have on the early stages of the visual system [32].

The model is not based on objects. A quick glance to Table 3 shows cloudy structures that have little to do with natural images (except e.g. those of the sky). In particular their appearance is rather fractionary, lacking real contours. However the model could provide an indication of which aspects of the visual processing depend only on the multiscaling properties and which ones are more dependent on spatial correlations.

By analyzing the finite size effects of synthetic images, we have concluded that the value of β is an essential feature of each natural image, which cannot be regarded as a fluctuation from a universal value. The generative model was also used to illustrate the meaning of the parameters β and \bar{s} .

The wavelet used in the generative model studied in this work was somewhat arbitrary. A better way to represent the multiscaling properties of natural images is to derive a wavelet basis from the image data set itself. When this is done, it is found that the coefficients of the wavelet expansion are scale-independent and weakly space-dependent, thus providing a quasi-optimal code for the image [32]. Their distribution for a given image is log-Poisson (eq. (6)), with exactly the same parameter β that would be obtained from the statistics of ϵ_r . This is a remarkable result, and supports our proposal that the visual system has adapted to the multiscaling properties of natural scenes and that its architecture contains, in particular, information about the log-Poisson multiplicative process.

Further equalization of these quasi-independent coefficients that follow the distribution given in eq. (6) could be an advantageous strategy for the visual system since it optimizes the mutual information between the source (visual stimuli) and the internal representation [34, 35]. Since the probability distributions of the quasi-independent coefficients depend on β this proposed equalization depends on the image

being processed.

To conclude, in this work we have established that the multiscaling properties of changes in contrast are a robust feature in natural images. The existence of this statistical regularity for single images has several implications for visual processing. This result is relevant because it implies a reduction of the entropy of the distribution probability of the ensemble of natural images. As a new statistical regularity is found, the set of images that can be considered as natural becomes more restricted. The fact that this property is present not only in ensembles but also in single images greatly reduces the entropy of the ensemble of natural images. Therefore its existence should be taken into account when modeling visual processing in the brain.

Acknowledgments

We are thankful to Angela del Pozo for her help during the initial stages of the preparation of this work. We are grateful to Hans van Hateren, some of whose images we used for the statistical analysis. Antonio Turiel is financially supported by an FPI grant from the Comunidad Autónoma de Madrid, Spain. This work was funded by a Spanish grant PB96-0047.

References

- [1] Barlow H. B., Possible principles underlying the transformation of sensory messages. in *Sensory Communication* (ed. Rosenblith W.) pp. 217. (M.I.T. Press, Cambridge MA, 1961).
- [2] Ruderman D. and Bialek W., Statistics of natural images: Scaling in the woods. *Phys. Rev. Lett.* **73**, 814 (1994)
- [3] Ruderman D., The statistics of natural images. *Network* **5**, 517-548 (1994)
- [4] Turiel A., Mato G., Parga N. and Nadal J.-P. Self-similarity properties of natural images. Proceedings of NIPS'97. Cambridge, MA: MIT Press (1998)
- [5] Turiel A., Mato G., Parga N. and Nadal J.-P. The self-similarity properties of natural images resemble those of turbulent flows. *Phys. Rev. Lett.* **80**, 1098-1101 (1998)
- [6] Turiel A. and Parga N., The multifractal structure of contrast changes in natural images: from sharp edges to textures. *Neural Computation* **12**, 858-883 (2000).
- [7] Turiel A., Parga N., Ruderman D. and Cronin T.W., Multiscaling and information content of natural color images. Submitted to *Phys. Rev. E* (1999).
- [8] Burton G.J. and Moorhead I.R., Color and spatial structure in natural scenes *Applied Optics* **26** 157-170 (1987).
- [9] Field D. J., Relations between statistics of natural images and the response properties of cortical cells. *J. Opt. Soc. Am. A* **4** 2379-2394 (1987).
- [10] R. Linsker. Self-organization in a perceptual network. *Computer*, **21** 105-117 (1988)
- [11] J. J. Atick. Could information theory provide an ecological theory of sensory processing. *NETWORK*, **3** 213-251 (1992)
- [12] J.H. van Hateren, Theoretical predictions of spatiotemporal receptive fields of fly lms, and experimental validation. *J. Comp. Physiology A*, **171** 157-170 (1992)
- [13] Zhaoping Li and J. J. Atick. Towards a theory of the striate cortex *Neural Computation*, **6** 127-146 (1994)
- [14] Field D. J., Scale-invariance and Self-similar “wavelet” transforms: an analysis of natural scenes and mammalian visual systems. In *Wavelets, Fractals, and Fourier Transforms* (ed. Farge M., Hunt J.C.R. and Vassilicos J.C.) pp. 151-193. (Clarendon Press, Oxford, 1993).
- [15] Lindberg T., “*Scale space theory in computer vision*” (Kluwer Academic Publishers, 1994).

- [16] Mallat S., Zhong S., Wavelet transform maxima and multiscale edges. In *Wavelets and their applications*. (eds. Ruskai M.B. et al) pp. 67-104. (Jones and Bartlett Publishers, Boston, 1991).
- [17] Zhen-Su She and Leveque E., Universal scaling laws in fully developed turbulence. *Phys. Rev. Lett.* **72**, 336-339 (1994).
- [18] Zhen-Su She and Waymire E.C., Quantized energy cascade and log-Poisson statistics in fully developed turbulence. *Phys. Rev. Lett.* **74**, 262-265 (1995).
- [19] Castaign B., Gagne Y. and Hopfinger, Velocity probability density functions of high Reynolds number turbulence *Physica (Amsterdam)* **46D**, 177 (1990).
- [20] Castaign B., The temperature of turbulent flows *J. Physique II (France)* **6**, 105-114 (1996).
- [21] Buccigrossi R.W. and Simoncelli E.P., Image Compression via Joint Statistical Characterization in the Wavelet Domain. *IEEE Trans Image Processing* **8**, 1688-1701, (1999).
- [22] Parisi G. and Frisch U., Fully developed turbulence and intermittency, in *Proc. of Intl. School on "Turbulence and Predictability in Geophysical fluid dynamics and climate dynamics"* (eds. Ghil M., Benzi R. and Parisi G.) pp. 84-87. (North-Holland, Amsterdam, 1985).
- [23] Mandelbrot B.B., *"Fractals: Form, Chance and Dimension"*. (Freeman, San Francisco, 1977).
- [24] Falconer K., *"Fractal Geometry: Mathematical Foundations and Applications"*. (John Wiley and sons, Chichester, 1990).
- [25] Benzi R., Ciliberto S., Baudet C., Ruiz Chavarria G. and Tripiccione C., *Europhys. Lett.* **24** 275-279 (1993)
- [26] Benzi R., Ciliberto S., Tripiccione R., Baudet C., Massaioli and Succi, Extended self-similarity in turbulent flows *Phys. Rev.* **E48**, R29 (1993)
- [27] Benzi R., Ciliberto S., Baudet C. and Ruiz Chavarria G., *Physica D* **80** 385-398 (1995)
- [28] van Hateren J.H. and van der Schaaf A., Independent component filters of natural images compared with simple cells in primary visual cortex. *Proc.R.Soc.Lond.* **B265**, 359-366 (1998)
- [29] Ruderman D., Origin of scaling in natural images *Vision Research* **37**, 3385-3398 (1997)
- [30] Field D.J., What is the goal of sensory coding?, *Neural Computation* **6** 559-601 (1994)

- [31] Benzi R., Biferale L., Ciliberto S., Struglia M.V. and Tripiccione R., Generalized scaling in fully developed turbulence, *Physica D* **96** 162-181 (1996)
- [32] Turiel A. and Parga N., The multifractal wavelet filter of natural images. Submitted to *Phys. Rev. Lett.* (1999)
- [33] Daubechies I., "*Ten Lectures on Wavelets*". CBMS-NSF Series in App. Math. *Capital City Press*. Montpelier, Vermont (1992)
- [34] Nadal J.-P. and Parga N., Nonlinear neurons in the low-noise limit: a factorial code maximizes information transfer *Network* **5** 565-581 (1994)
- [35] Nadal J.-P., Brunel N. and Parga N., Nonlinear feedforward networks with stochastic outputs: infomax implies redundancy reduction. *Network* **9** 1-11 (1998)
- [36] Ahmed B., Allison J.D., Douglas R.J. and Martin K.A.C., Intracellular study of the contrast-dependence of neuronal activity in cat visual cortex *Cerebral Cortex* **7** 559-570 (1997)
- [37] Carandini M. and Ferster D., A tonic hyperpolarization underlying contrast adaptation in cat visul cortex *Science* **276** 949-952 (1997)

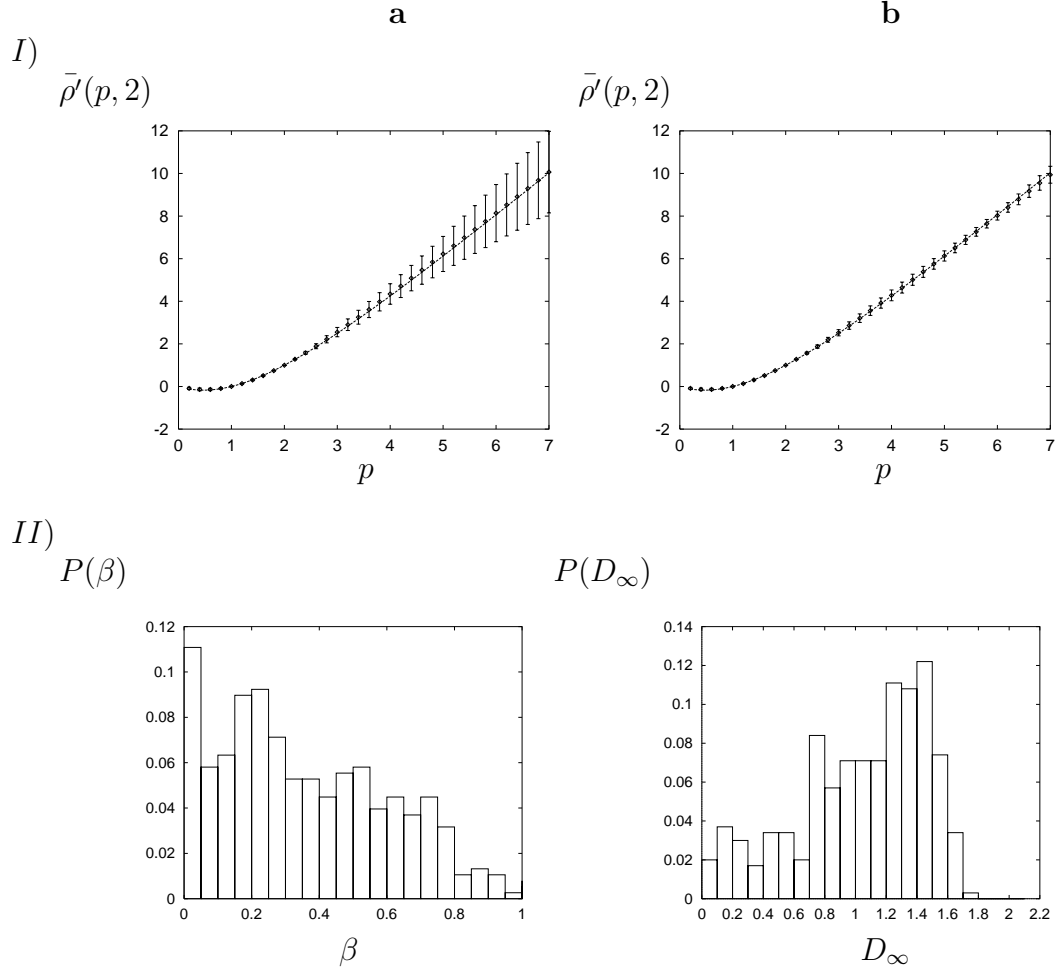


Figure 4: Test of the log-Poisson model for the 400 images. Ia) The mean of the $\rho'(p, 2)$'s over the 400 images. Ib) The mean of the $\rho(p, 2)$'s for the 375 best images. Again, for a) and b) the diamonds represent the mean of $\rho'(p, 2)$ and the error bars are twice the standard deviation. The dashed line represents $\rho^{0.5}(p, 2)$. IIa) Histogram of values of β for the 375 selected images. IIb) Histogram of values of D_∞ for the 290 images with D_∞ in the range $[0:2]$

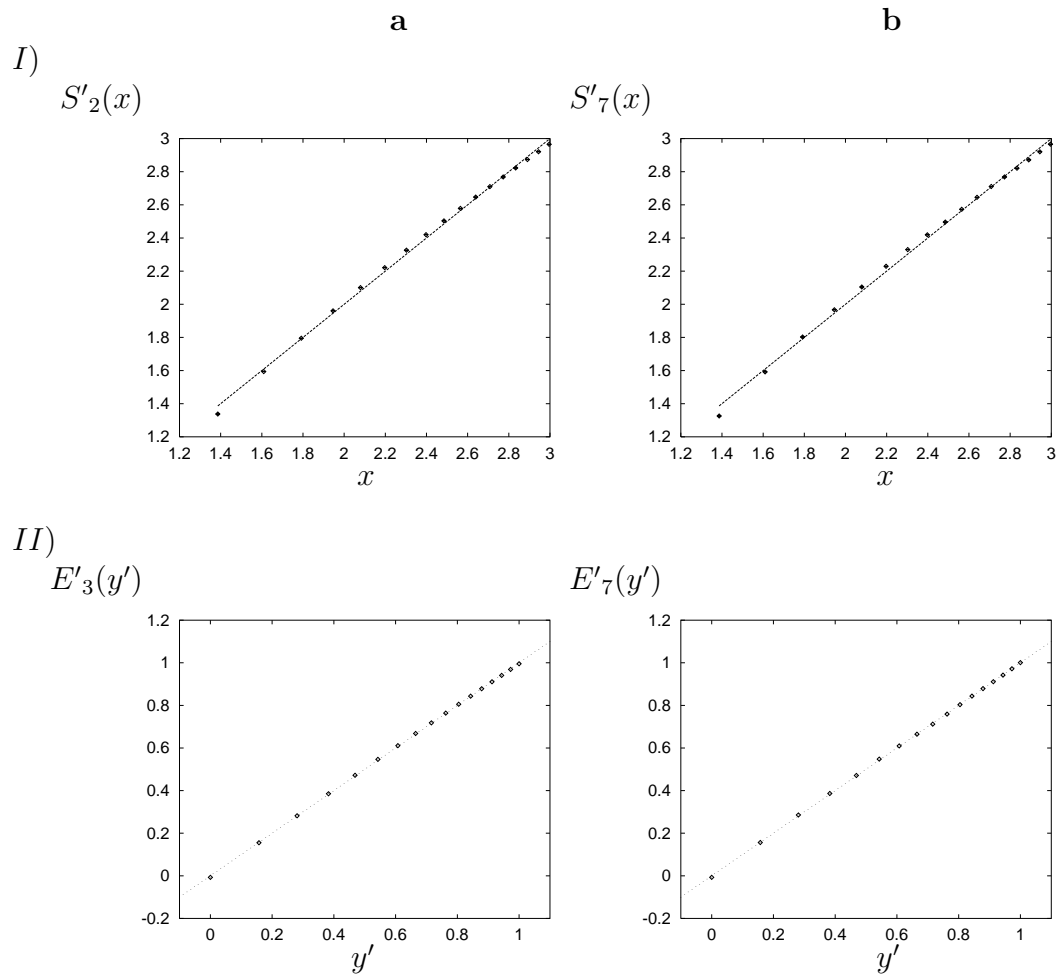


Figure 5: Test of SS and ESS for the whole image data set (400 images). I) SS test for the moments of order two (a) and seven (b). The dashed line represents $f(x) = x$. II) ESS test for the moments of order three (a) and seven (b). The dotted line represents $f(y')=y'$.

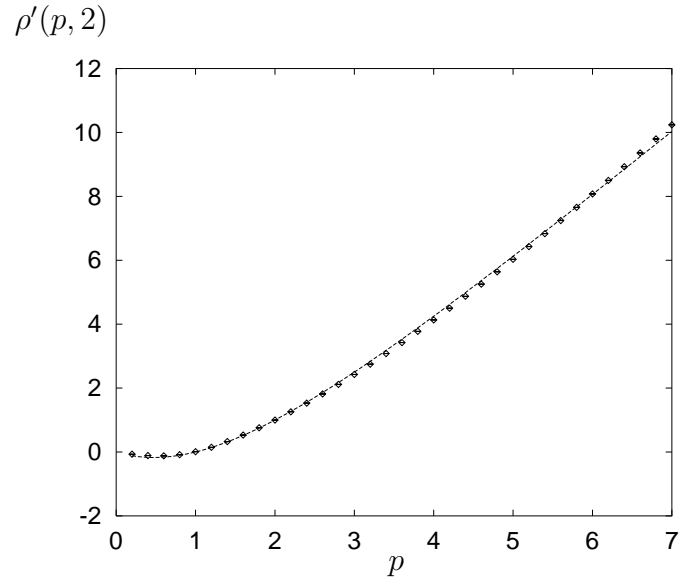


Figure 6: Test of the log-Poisson model for the whole data set.

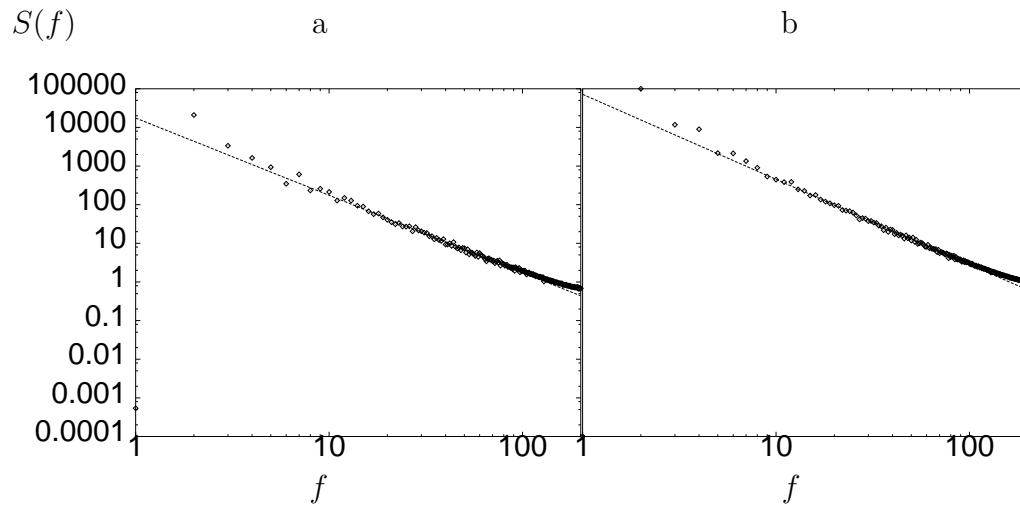


Figure 7: log-log plot of the power spectrum along the a) horizontal and b) vertical directions for a 512×512 image produced with the generative model. The straight lines correspond to $1/f^2$ fits; the horizontal axes are given in cycles *per* image.

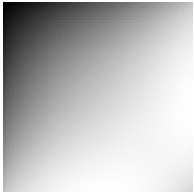
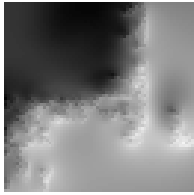
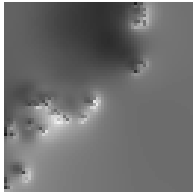
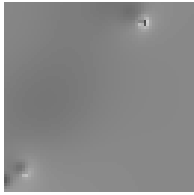
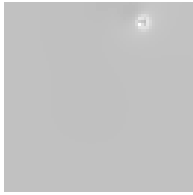
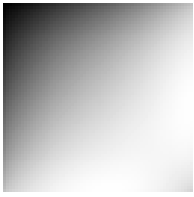
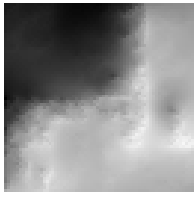
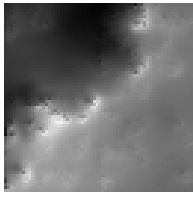
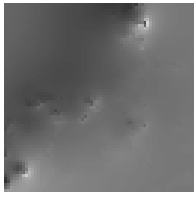
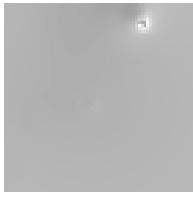
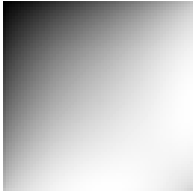
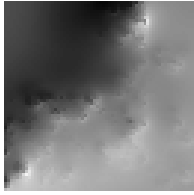
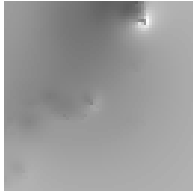
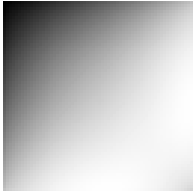
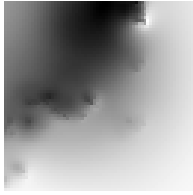
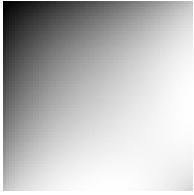
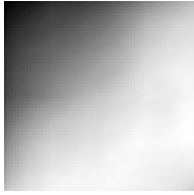
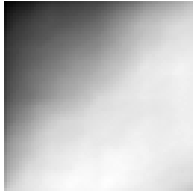
	$\bar{s} = 0.0$ ($D_\infty = 2.0$)	$\bar{s} = 0.5$ ($D_\infty = 1.5$)	$\bar{s} = 1.0$ ($D_\infty = 1.0$)	$\bar{s} = 1.5$ ($D_\infty = 0.5$)	$\bar{s} = 2.0$ ($D_\infty = 0.0$)
$\beta = 0.0$					
$\beta = 0.2$					
$\beta = 0.4$					
$\beta = 0.6$					
$\beta = 0.8$					

Table 3: Catalogue of synthetic images. The case $\beta = 1$ is not shown because the images are like those for $\bar{s} = 0$ (see text)

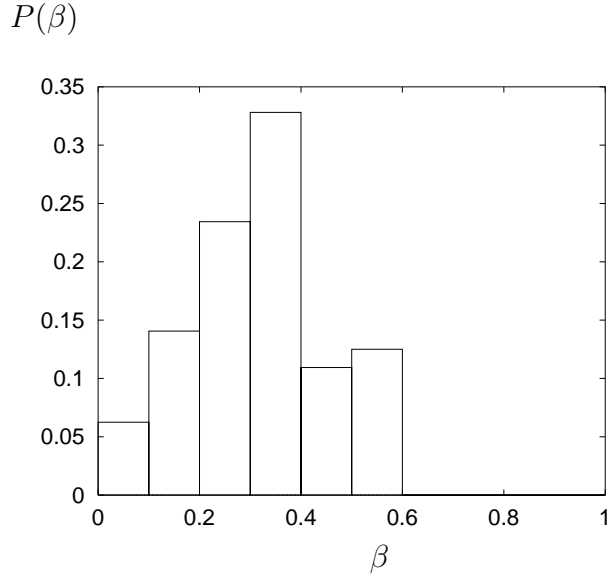


Figure 8: Generative model. Histogram of β for the 32 256×256 synthetic images (and two directions) with a theoretical $\beta = 0.40$

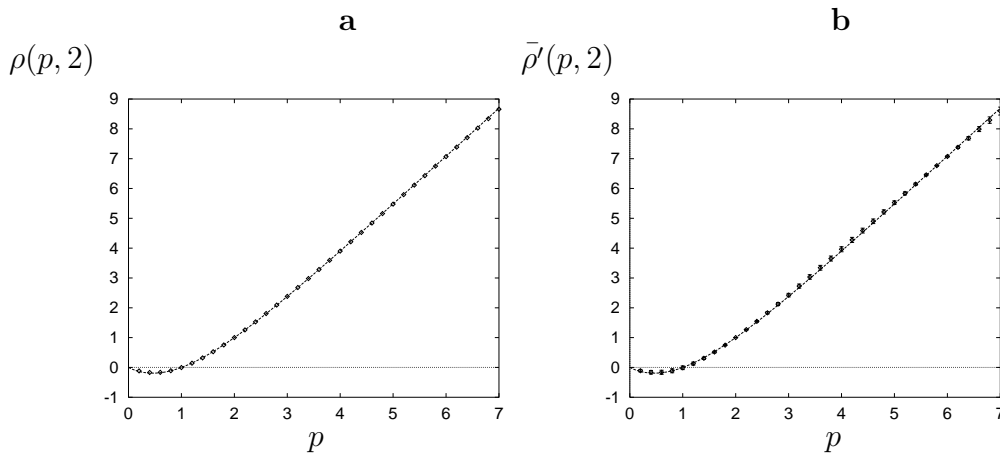


Figure 9: Test of the log-Poisson multiplicative process for the generative model. a) $\rho(p, 2)$ for the averaged moments of the whole ensemble of 32 256×256 images. The dashed line corresponds to the ESS exponents predicted by the log-Poisson model for $\beta = 0.38$. b) The mean of $\rho'(p, 2)$ over the 32 synthetic images and the two directions, where now $\rho'(p, 2)$ has been normalized to $\beta = 0.38$. The dashed line represents $\rho^{0.38}(p, 2)$, the log-Poisson $\rho(p, 2)$ with $\beta = 0.38$. The error bars are of the size of the data points.